PAPER • OPEN ACCESS

Towards accurate modeling of the multidimensional magnetic particle imaging physics

New Journal of Physics
The open access journal at the forefront of physics

Deutsche Physikalische Gesellschaft DPG
IOP Institute of Physics

Published in partnership with: Deutsche Physikalische Gesellschaft and the Institute of Physics

OPEN ACCESS

RECEIVED
4 May 2019

REVISED
16 September 2019

ACCEPTED FOR PUBLICATION
30 September 2019

PUBLISHED
15 October 2019

PAPER

Towards accurate modeling of the multidimensional magnetic particle imaging physics

T Kluth[1], **P Szwargulski**[2,3] and **T Knopp**[2,3,4]

[1] Center for Industrial Mathematics, University of Bremen, Germany
[2] Section for Biomedical Imaging, University Medical Center Hamburg-Eppendorf, Germany
[3] Institute for Biomedical Imaging, Hamburg University of Technology, Germany
[4] Author to whom any correspondence should be addressed.

E-mail: tkluth@math.uni-bremen.de **and** t.knopp@uke.de

Keywords: magnetic particle imaging, ferrofluids, magnetic nanoparticles, Fokker–Planck equation

Abstract

The image reconstruction problem of the tomographic imaging technique magnetic particle imaging (MPI) requires the solution of a linear inverse problem. One prerequisite for this task is that the imaging operator that describes the mapping between the tomographic image and the measured signal is accurately known. For 2D and 3D excitation patterns, it is common to measure the system matrix in a calibration procedure, that is both, very time consuming and adds noise to the operator. The need for measuring the system matrix is due to the lack of an accurate model that is capable of describing the nanoparticles' magnetization behavior in the MPI setup. Within this work we exploit a physical model that is based on Néel rotation for large particle ensembles and we find model parameters that describe measured 2D MPI data with much higher precision than state of the art MPI models. With phantom experiments we show that the simulated system matrix can be used for image reconstruction and reduces artifacts due to model-mismatch considerably.

1. Introduction

Tomographic imaging techniques play a major role in medical diagnostics and treatment. In 2005, a new method called magnetic particle imaging (MPI) was introduced [1], which allows to image magnetic nanoparticles (MNPs) with high sensitivity and high spatio-temporal resolution. In contrast to magnetic resonance imaging, the contrast in MPI is positive and the reconstructed images are quantitative. With these properties MPI is an interesting candidate for various medical applications ranging from vascular imaging [2–5] to targeted imaging [6].

Signal encoding in MPI is achieved by exciting the MNPs with one or several homogeneous excitation fields with a frequency in the kHz region [7]. The MNPs respond with a change of their magnetization, which is measured with one or multiple receive coils. Spatial encoding is achieved by superimposing a static gradient field leading to a spatially dependent magnetization response of the MNPs to the excitation field. In ferrofluids the change of the particle magnetization is enabled by two different well studied dynamic processes: the Brownian rotation describes the mechanical alignment of the entire particle with a change of the magnetic field whereas Néel rotation describes the alignment of the particle's inner magnetic moment. Note that due to the continuous excitation the system does not relax in MPI. The corresponding dynamic models are well studied in the context of applications like for example magnetic storage media [8] and they were also considered for MPI since at least one decade (see also the recent survey [9]). In the context of MPI the dynamics were initially studied by Weizenecker *et al* [10] in terms of stochastic ordinary differential equations. A first attempt to Brownian rotation via the Fokker–Planck equation was presented by Yoshida and Enpuku for 1D excitation patterns [11] followed by further works in this direction [12–16]. More recently, the Fokker–Planck equation of a coupled Brownian and Néel model was investigated regarding their representation in spherical harmonics [17]. Different MNPs are often categorized by the dominating mechanism. For example, Resovist's magnetization behavior is mainly

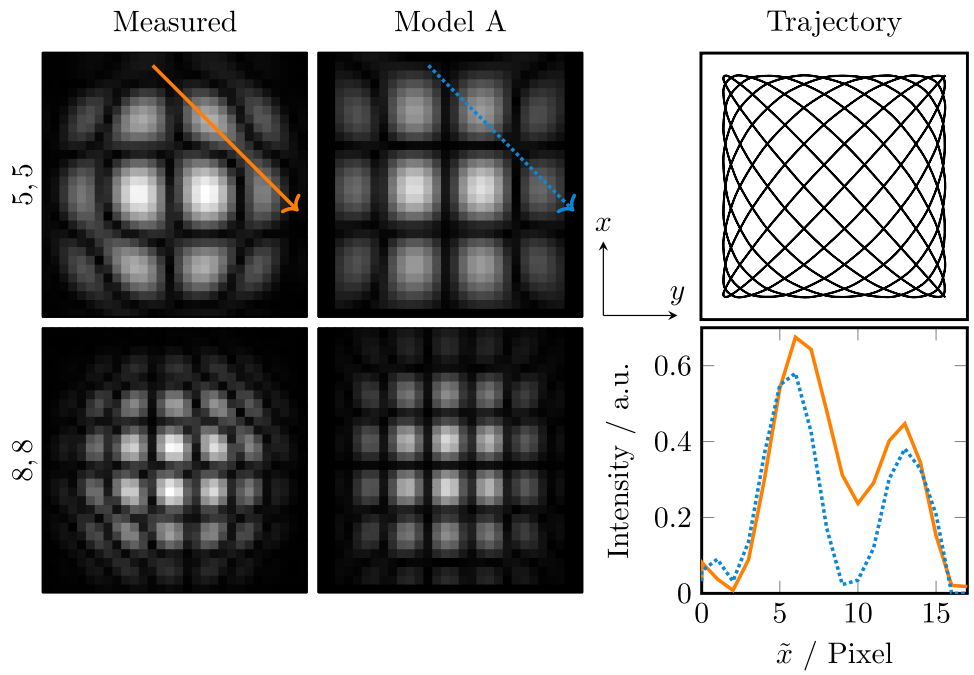

Figure 1. Imperfections of the equilibrium model compared to measured data. Absolute of two selected frequency components (denoted by mixing factors m_x and m_y) are shown in the first and second row. The measured system matrix using the unmodified particle solution is shown in the first column while the simulated matrix based on the equilibrium model (model A) is shown in the second column. In the last column the sampling pattern (top) and line profiles (bottom) through two of the wave hills marked in system matrix images for $m_x = m_y = 5$ are shown.

determined by Néel rotation, whereas a frequency-dependent (with respect to the applied field) influence of Brownian rotation can be observed [18]. Furthermore, the orientation of the particles' easy axis significantly influences the magnetization behavior due to the Néel rotation [19]. The still incomplete nature of models for imaging in MPI has motivated an increasing number of studies in the context of Brownian and Néel rotations for one-dimensional [12, 20–23] as well as two-dimensional [24] MPI excitation patterns.

In order to reconstruct an image of the MNP concentration, the physical processes during the MPI experiment need to be inverted. Mathematically, this involves the solution of an ill-posed linear system of equations [25]. One prerequisite for image reconstruction is that the system matrix is accurately known. Since its very first introduction in [1], the system matrix is measured in a data-driven calibration procedure by determining the response of the system to a small delta sample that is shifted through the imaging volume. The main advantage of this method is that it takes all physical effects of the imaging process into account but it has also two major drawbacks: the measured system matrix includes noise and the calibration procedure is very time consuming lasting up to several days [26]. These drawbacks motivated the development of methods determining the MPI system matrix based on physical models. While the initial model-based results in [27] and [28] were promising, model-based reconstruction based on the used *equilibrium model* denoting the simplified model which assumes infinitely fast relaxation leads to worse image quality than the data driven approach [29]. This is why the latter is still the method of choice in almost all publications since 2010 that use multidimensional excitation patterns in the context of image reconstruction. For 1D excitation, which includes 2D and 3D Cartesian like sampling patterns [30], model-based reconstruction has been established in various works since it enables simple time-signal based reconstruction [31].

Within this work we investigate the question why the simple equilibrium model fails to accurately describe the MPI system matrix for 2D Lissajous type excitation patterns. As a motivating example we consider a system matrix measured along a 2D Lissajous trajectory (frequency ratio 16/17, details are outlined in section 6). Figure 1 shows two selected rows of the 2D MPI system matrix and compares the measurement with the equilibrium-based simulation. One can see that the simulation matches quite well the basic structure of the matrix rows, which are consisting of wave patterns that share high similarity to 2D tensor products of Chebyshev polynomials [32]. However, when taking a closer look one can identify various differences that lead to larger numerical deviations. In particular we want to highlight two qualitative effects. First, the wave hills are merging in outer regions of the field-of-view (FoV), i.e. in regions where the simulation has a zero-crossing there is a non-zero value in the measured one. This effect is clearly visible in a line profile through two neighbouring wave hills shown in figure 1. Second, one can see a tilting of the outer wave structures in outer regions of the FoV. The goal

of this work is to simulate these effects using a physical model that takes Néel rotation of the particles' magnetic moments into account.

2. Methods

We consider a general MPI imaging experiment where the particles are located in the MPI scanner and the change of the particle magnetization is measured using induction coils. Then the voltage induced in a receive coil with sensitivity profile $p : \mathbb{R}^3 \to \mathbb{R}^3$ in m^{-1} is given by

$$\tilde{v}(t) = -\mu_0 \int_\Omega c(x) p(x)^\mathsf{T} \frac{\partial}{\partial t} \bar{m}(x, t) \; \mathrm{d}x$$

in V where $c : \Omega \to \mathbb{R}_0^+$ in $\mathrm{mol\,l}^{-1}$ is the concentration of the magnetic nanoparticles, $\bar{m} : \mathbb{R}^3 \times [0, T] \to \mathbb{R}^3$ in $10^{-3}\,\mathrm{Am}^2\,\mathrm{mol}^{-1}$ is the molar mean magnetic moment of particles and $\Omega \subset \mathbb{R}^3$ is the imaging volume. The mean magnetic moment $\bar{m}(x, t)$ depends on the applied magnetic field $H_{\mathrm{app}} : \mathbb{R}^3 \times [0, T] \to \mathbb{R}^3$ in Am^{-1}, which is usually a T-periodic function with period T along the time dimension. In MPI a static selection field $H_{\mathrm{S}} : \mathbb{R}^3 \to \mathbb{R}^3$ is combined with a dynamic drive field $H_{\mathrm{D}} : \mathbb{R}^3 \times [0, T] \to \mathbb{R}^3$, i.e. $H_{\mathrm{app}}(x, t) = H_{\mathrm{S}}(x) + H_{\mathrm{D}}(x, t)$. The induced signal is analogously filtered to remove the main contribution of the direct feedthrough. It is represented by a convolution with a T-periodic filter kernel a: $\mathbb{R} \to \mathbb{R}$ yielding the signal $v = a * \tilde{v}$. Therefore, v is T-periodic as well and can be expanded into a Fourier series with coefficients

$$\hat{v}_k = -\hat{a}_k \frac{\mu_0}{T} \int_\Omega c(x) p(x)^\mathsf{T} \int_0^T \left(\frac{\partial}{\partial t} \bar{m}(x, t) \right) \mathrm{e}^{-2\pi \mathrm{i} t k / T} \; \mathrm{d}t \; \mathrm{d}x$$

for $k \in \mathbb{N}_0$ and the conjugate complex $\hat{v}_{-k} = \overline{\hat{v}_k}$. This formulation is commonly used, since the signal at the excitation frequencies is blocked using an analog band-stop filter prior to the signal digitization. With $s_k(x) := -\hat{a}_k \frac{\mu_0}{T} \int_0^T p(x)^\mathsf{T} \frac{\partial}{\partial t} \bar{m}(x, t) \mathrm{e}^{-2\pi \mathrm{i} t k / T} \; \mathrm{d}t$ we can bring this into the standard notation

$$\hat{v}_k = \int_\Omega c(x) s_k(x) \; \mathrm{d}x,$$

where s_k: $\mathbb{R}^3 \to \mathbb{C}$ is the system function that we already discussed in figure 1. When measuring the system function at discrete positions $x_l, l = 1, \ldots, N$, and with a certain sampling rate in time, one obtains the MPI system matrix $S = (s_k(x_l))_{k=0,\ldots,K; l = 1,\ldots,N}$ storing the Fourier transformed measurements in the respective columns. In this work we will consider both modeled system matrices S^{Mod} as well as measures system matrices S^{Cal} that are obtained by moving a small delta sample through the FoV. In case of multiple receive channels, the corresponding system matrices can be stacked to arrive at a joint linear system of equation; see for example [33] for a formal definition.

3. Particle models

Since H_{app} and p can be easily modeled using the Biot–Savart law and a can either be measured or fitted [28], we focus on modeling the particles' mean magnetic moment behavior. We first consider the equilibrium model that can be derived under the assumption that the particles are always in thermal equilibrium in which case $\bar{m}$ directly follows the applied field H_{app}. We refer to it as *model A* which is given by

$$\bar{m}(x, t) = m_0 \mathcal{L}_\beta(|H_{\mathrm{app}}(x, t)|) \frac{H_{\mathrm{app}}(x, t)}{|H_{\mathrm{app}}(x, t)|}, \tag{1}$$

where $\mathcal{L}_\beta : \mathbb{R} \to \mathbb{R}$ is given in terms of the Langevin function by the following:

$$\mathcal{L}_\beta(z) = \left(\coth(\beta z) - \frac{1}{\beta z} \right) \tag{2}$$

for $m_0, \beta > 0$. Both $m_0 = V_{\mathrm{C}} M_{\mathrm{S}}$ and $\beta = \frac{\mu_0 V_{\mathrm{C}} M_{\mathrm{S}}}{k_{\mathrm{B}} T_{\mathrm{B}}}$ with $V_{\mathrm{C}} = \frac{1}{6}\pi D^3$ depend on the particle core diameter D in a cubic fashion.

Since we have already seen that the equilibrium model is not accurate enough for modeling the nanoparticles' behavior in an MPI experiments we next consider a more appropriate model that takes magnetization dynamics into account. There are basically two different approaches, one can either consider the problem on a micromagnetic level for individual particles and solve the Langevin equation corresponding to the Landau–Lifschitz–Gilbert equation for a sufficiently large number of particles to obtain a reasonable estimate for the mean. Alternatively, one can take a comprehensive view and solve the Fokker–Planck equation for a probability distribution representing an entire ensemble of nanoparticles in terms of a parabolic partial differential equation. The latter approach benefits from efficient and more accurate solutions when aiming for a

mean computation [17] as determining the mean from the Langevin equation requires a large number of particle simulations.

The second case which we refer to as model B is based on the latter approach which determines the mean magnetic moment via the probability density function $f : S^2 \times \Omega \times [0,\ T] \to \mathbb{R}_0^+$ which is the solution to the corresponding Fokker–Planck equation where S^2 is the surface of the sphere in $\mathbb{R}^3$. The mean is then given by

$$\bar{m}(x,\ t) = m_0 \int_{S^2} mf\,(m,\ x,\ t)\ \ \mathrm{d}m, \tag{3}$$

where f is the solution to the following specific case of a convection–diffusion equation on the sphere

$$\frac{\partial}{\partial t} f = \mathrm{div}_{S^2}\left(\frac{1}{2\tau}\nabla_{S^2} f\right) - \mathrm{div}_{S^2}(bf), \tag{4}$$

where $\tau > 0$ is the relaxation time constant and the (velocity) field $b : S^2 \times \mathbb{R}^3 \times S^2 \to \mathbb{R}^3$ given by

$$b(m,\ H_{\mathrm{app}},\ n) = p_1 H_{\mathrm{app}} \times m + p_2(m \times H_{\mathrm{app}}) \times m + p_3(n \cdot m)n \times m + p_4(n \cdot m)(m \times n) \times m, \tag{5}$$

where $p_i \geqslant 0$, $i = 1,\ldots,4$, are physical constants and $n \in S^2$ is the easy axis of the particles. Differentiation in terms of gradient ∇_{S^2} and divergence div_{S^2} is considered with respect to the surface S^2. The Euclidean scalar product of $\mathbb{R}^3$ is denoted by $n \cdot m$. The specific structure of the Fokker–Planck equation is due to the independent consideration of Brownian and Néel rotation model as it was observed for common tracer that one mechanism can be dominant [18]. For a detailed discussion of the relationship between Fokker–Planck equation and Langevin equations for Brownian and Néel rotation we refer to the survey [9]. A pure Néel rotation including anisotropy is given by $p_1 = \tilde{\gamma}\mu_0$, $p_2 = \tilde{\gamma}\alpha\mu_0$, $p_3 = 2\tilde{\gamma}\frac{K_{\mathrm{anis}}}{M_{\mathrm{S}}}$, $p_4 = 2\tilde{\gamma}\frac{K_{\mathrm{anis}}}{M_{\mathrm{S}}}$, and $\tau = \frac{V_{\mathrm{C}} M_{\mathrm{S}}}{2k_{\mathrm{B}} T_{\mathrm{B}} \tilde{\gamma}\alpha}\left(\tilde{\gamma} = \frac{\gamma}{1+\alpha^2}\right)$. We note that the parabolic partial differential equation in (4) has no dependence on derivatives with respect to the spatial variable x. It can thus be considered as parametric with respect to x.

In the following we use the Néel rotation model as it includes the particle anisotropy. Here we distinguish the following three cases to identify the relevant modeling aspects:

Néel rotation model without anisotropy, i.e. $p_3 = p_4 = 0$ in (5).

Néel rotation model including anisotropy, i.e. it includes all summands in (5) for a given easy axis $n \in S^2$.

Néel rotation model including a space-dependent anisotropy which is related to the local structure of the magnetic field, i.e. n: $\Omega \to S^2$ and p_3, p_4: $\Omega \to \mathbb{R}_0^+$. Here, we use $n(x) = \frac{H_{\mathrm{S}}(x)}{|\,H_{\mathrm{S}}(x)\,|}$ and $K_{\mathrm{anis}}(x) = g_{K_{\mathrm{anis}}}|H_{\mathrm{S}}(x)|/h$ with anisotropy gradient $g_{K_{\mathrm{anis}}}$ and $h = \max_{x\in\Omega}|H_{\mathrm{S}}(x)|$ resulting in p_3 and p_4.

Following the approach in [17] the numerical solution of (4) is obtained as follows: we consider an initial value $f\,(m,\ x,\ 0) = f_0(m,\ x)$ with $f_0(\cdot,x) \geqslant 0$ and $\|f_0(\cdot,x)\|_{L^1(S^2)} = 1$ for any $x \in \Omega$. A semi-discrete Cauchy problem is obtained via discretization in non-normalized spherical harmonics $\{Y_l^\kappa \mid l \in \mathbb{N}_0,\ \kappa \in \{-l,\ldots,l\}\}$ (with respect to m while considering a rotated problem using a rotation matrix $R \in \mathbb{R}^{3\times 3}$ such that $Rn = e_3$), which yields a first order ordinary differential equation system for any $x \in \Omega$. The initial value problem is then solved on a time interval covering multiple periods of the excitation pattern while using a uniform initial value (for any $x \in \Omega$). The numerical solution is obtained via a variable order, variable step solver using Matlab's built-in function `ode15s`. The last period of the solution is then used for further investigations. The mean magnetic moment can then be determined directly via linear combinations of the coefficients corresponding to the spherical harmonics Y_1^0, Y_1^1, and Y_1^{-1}, which is subsequently rotated back.

4. Distance measure

For quantifying the accuracy of a model we express the frequency index k in terms of the mixing orders m_x, m_y [34] fulfilling

$$k(m_x,\ m_y) = m_x N_{\mathrm{Dens}} + m_y(N_{\mathrm{Dens}} + 1). \tag{6}$$

Here, N_{Dens} is the parameter that controls the density of the Lissajous sampling pattern and for each k the factors m_x and m_y with the smallest absolute value fulfilling (6) are considered. Now with $S^{\mathrm{Cal}}_{k(m_x,m_y)}$ being the measured and $S^{\mathrm{Mod}}_{k(m_x,m_y)}$ being the modeled system matrix row we consider the normalized root mean square error (NRMSE)

$$\varepsilon(S_k^{\mathrm{Cal}},\ S_k^{\mathrm{Mod}}) = \frac{\frac{1}{\sqrt{N}}\ \|S_k^{\mathrm{Cal}} - S_k^{\mathrm{Mod}}\|_2}{\|S_k^{\mathrm{Cal}}\|_\infty}, \tag{7}$$

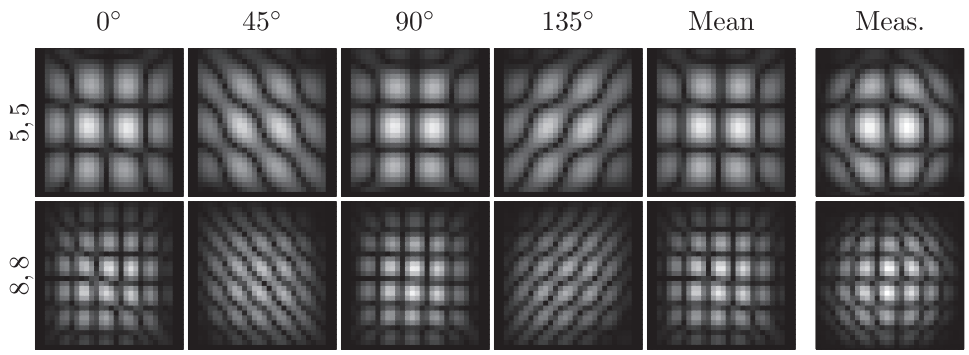

Figure 2. Selected frequency components of modeled system matrices using the Néel model with anisotropy constant 625 Jm^{-3} and a homogeneous easy axis for 4 different orientations (columns 1–4). Column 5 shows the mean over all easy axes while column 6 shows the measured system matrix for reference.

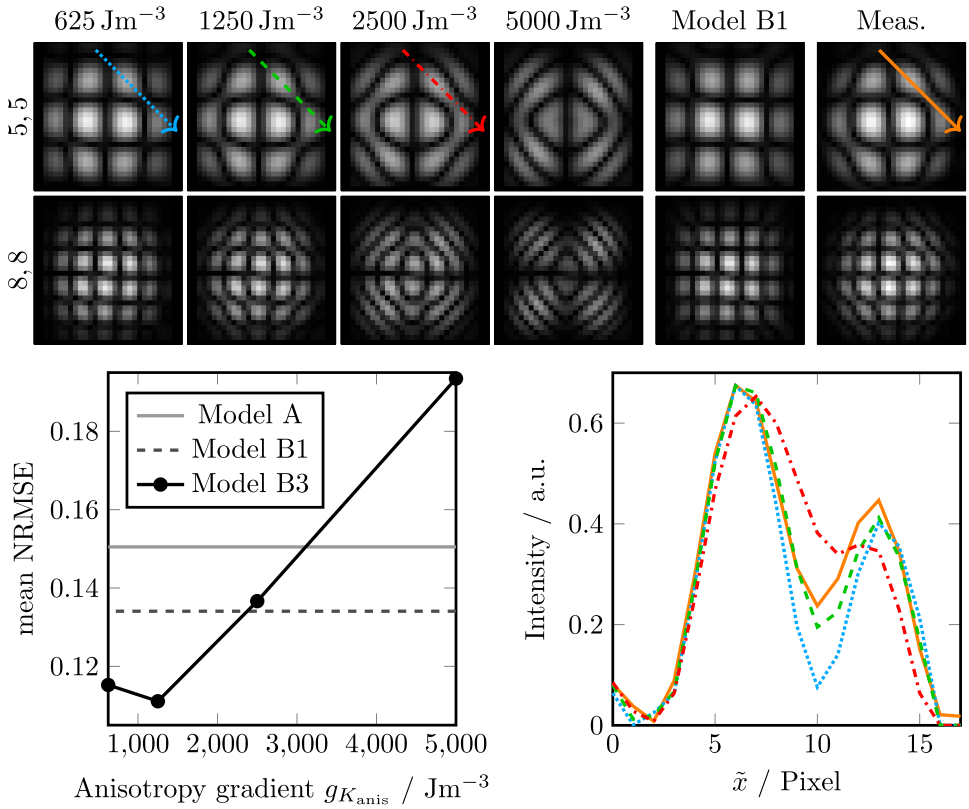

Figure 3. Selected frequency components of modeled system matrices using the Néel model B3 with anisotropy gradients $g_{K_{\mathrm{anis}}}$ ranging from 625 Jm^{-3} to 5000 Jm^{-3} (columns 1–4; left to right). Column 5 shows the modeled system matrix using the Néel model B1 without anisotropy while column 6 shows the measured system matrix for reference. Below the images of the frequency components, the mean NRMSE between the model and the measurement is shown (left). In the lower right, line profiles through two of the wave hills for $m_x = m_y = 5$ are shown for selected system matrices.

where we decided to use the infinity norm for normalization. In addition to this per-row metric we consider the mean NRMSE over $m_x = 0, \ldots, M_x$ and $m_y = 0, \ldots, M_y$ where M_x, $M_y \in \mathbb{N}$ are upper bounds for the mixing order.

5. Image reconstruction

For image reconstruction we use the standard framework [35] that applies the iterative Kaczmarz algorithm augmented by Tikhonov regularization, a positivity constraint, and background subtraction [36]. We apply standard SNR thresholding where matrix rows with low SNR (<1.5) are removed prior to reconstruction. In

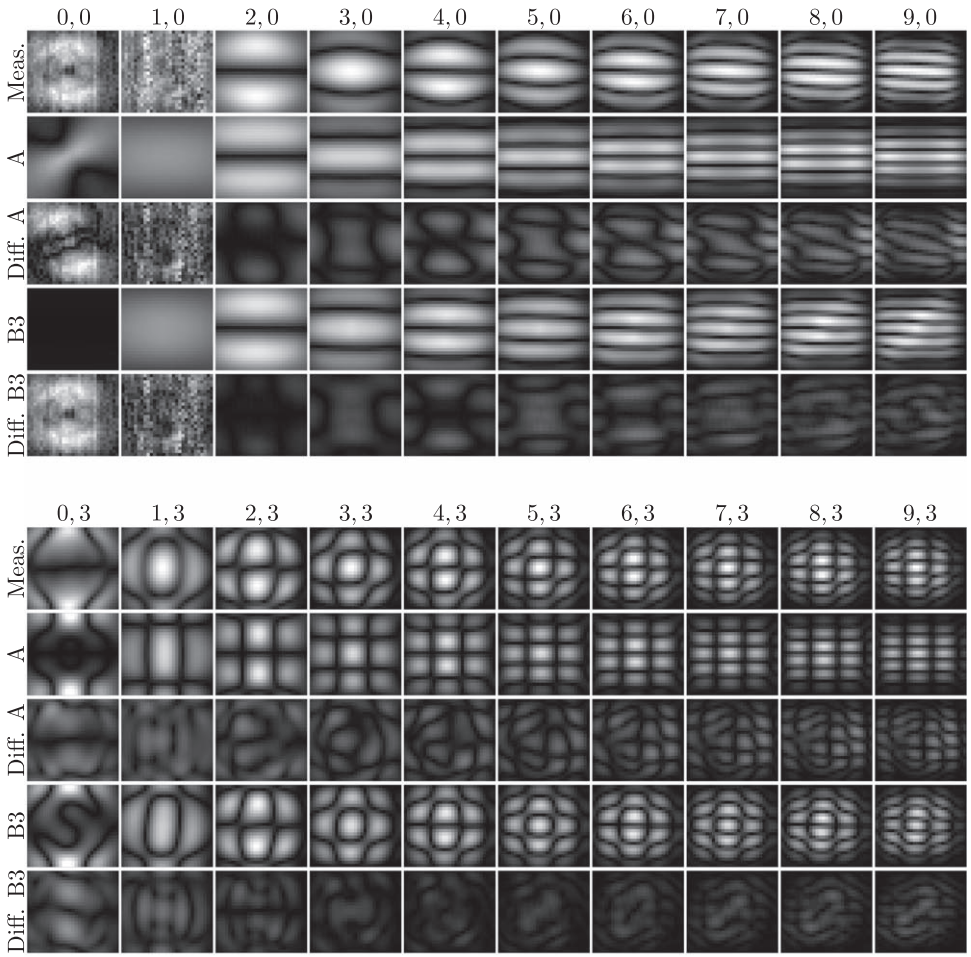

Figure 4. Comparison of measured and modeled system matrices for the equilibrium model A and the Néel model B3 for $g_{K_{\text{anis}}} = 1250\ \text{Jm}^{-3}$. Shown are frequency components for combinations of $m_x = 0, \ldots, 9$ and $m_y = 0, 3$. Below in the 'Diff.' rows of the respective model, the absolute difference between measurement and model is shown.

addition we apply a second way of matrix row filtering. The idea is to select only those matrix rows of the modeled system matrices, which deviate only marginal from the measured one. Let $\Theta \in [0,1]$ be a predefined threshold. Then, we choose matrix rows k where $\varepsilon(S_k^{\text{Cal}}, S_k^{\text{Mod}}) < \Theta$. The parameter Θ can now be used to trade of between inaccuracies due to the model/measurement mismatch and a loss off spatial resolution that happens when only few system matrix rows are selected for reconstruction. The total number of matrix rows selected for reconstruction will be denoted by W.

6. Experimental setup

Experimental data were measured with a preclinical MPI scanner (Bruker, Ettlingen) using field-free-point (FFP) excitation patterns. In all experiments a 2D cosine excitation ($N_{\text{Dens}} = 16, f_0 = 2.5/6$ MHz) within the xy-plane of the scanner was applied with excitation-field amplitudes $A_x = A_y = 12\ \text{mT}\mu_0^{-1}$ and $1\ \text{Tm}^{-1}\mu_0^{-1}$ selection field gradient within the xy-plane. The resulting area covered by the FFP is of size $24 \times 24\ \text{mm}^2$.

The system matrix was measured by shifting a $1\ \text{mm}^3$ cubic delta sample of perimag (micromod, Rostock) to 30×30 positions covering a FoV of size $30 \times 30\ \text{mm}^2$ (1 mm step size). A particle phantom consisting of three rods with 0.7 mm in diameter is prepared using the same tracer of the same concentration as the delta sample. The phantom is shown in figure 6.

7. Model parameter selection

The considered models each have several parameters that are a-priori unknown. Furthermore, the computation time of one system matrix for one parameter instance and a time interval covering two periods of the excitation signal is approximately up to 12 h when using 24 cores in parallel (2×Intel(R) Xeon(R) CPU E5-2687W v4 @

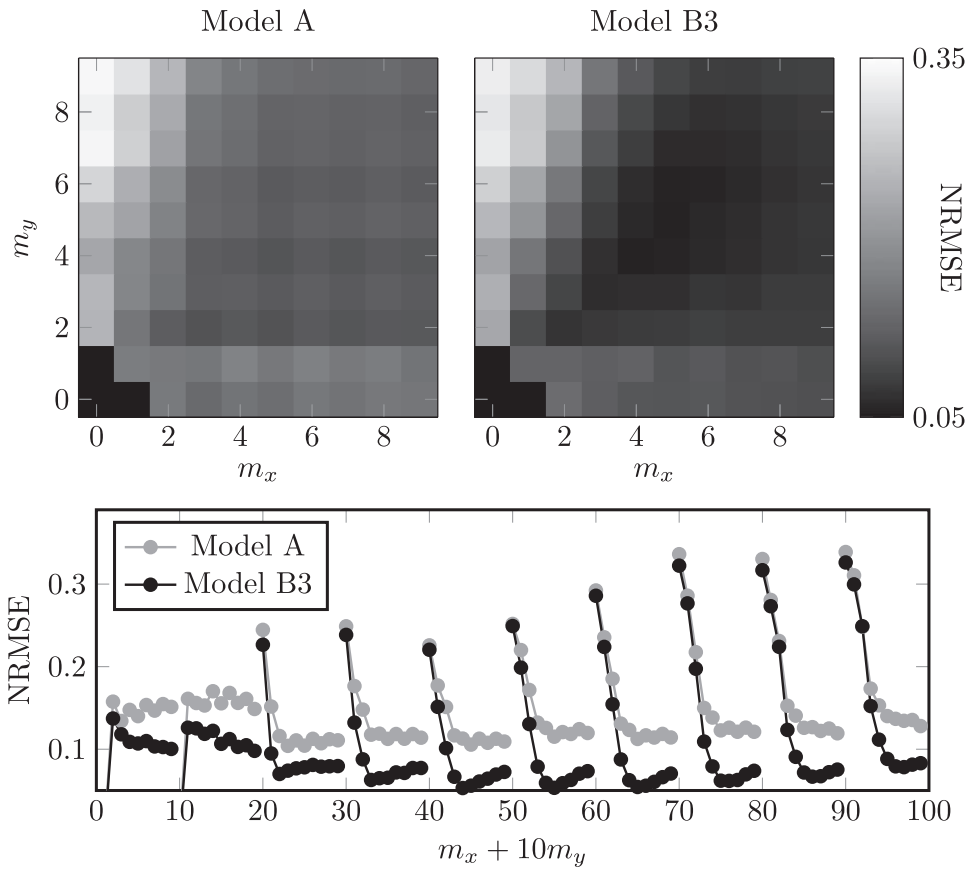

Figure 5. Error of the modeled system matrices (A and B3) shown in figure 4. The error is shown in two individual gray scale images (top) and for direct comparison in a flattened plot (bottom).

3.00GHz). Since the simulation of the models requires a significant time, it is challenging to apply for example gradient-based optimization techniques to the continuous parameter space. Therefore, we calculate system matrices for a finite number of settings and perform a subsequent discrete optimization.

Model A as well as models B1–B3 require as input the particle core diameter D. We simulated the equilibrium model for $D \in \{20\,, 25, 30\ \text{nm}\}$ and found in initial tests that the system matrices with $D = 20$ nm fitted best in all model cases and are therefore considered $D = 20$ nm for further investigations. For the Néel model B2 we consider a spatially homogeneous easy axis distribution $n(\theta) = (\cos(\theta),\ \sin(\theta))^{\mathsf{T}}$ and orientations $\theta \in \{0°,\ 45°,\ 90°,\ 135°\}$. In this case the anisotropy constant is chosen as $K_{\text{anis}} = 625\ \text{Jm}^{-3}$.

For the inhomogeneous case B3 we consider an easy axis $n(x) = n(x) = \frac{H_S(x)}{|\,H_S(x)\,|}$ and $K_{\text{anis}}(x) = g_{K_{\text{anis}}}|H_S(x)|/h$ where we chose $g_{K_{\text{anis}}} \in \{625,\ 1250,\ 2500,\ 5000\}\,\text{Jm}^{-3}$ and $h = \max_{x\in\Omega}|H_S(x)|$. Thus, the easy axis is parallel to the selection field vector and the effective anisotropy increases when increasing the distance to the FFP of the selection field.

In all cases, wherever applicable, we used the damping parameter $\alpha = 0.1$, the gyromagnetic ratio $\gamma = 1.7 \times 10^{11}\ \text{rad s}^{-1}$, and the saturation magnetization $M_S = 474\,000\ \text{Jm}^{-3}\,\text{T}^{-1}$.

8. Results

First, we consider the Néel model B2 with spatially homogeneous anisotropy distribution and homogeneous easy axis. Selected rows of simulated system matrices are shown in figure 2. One can see that the angles 0° and 90° do not change the shape of the patterns compared to the equilibrium model. However, for 45° and 135° one can see the desired effect that the patterns are tilted in one direction, which is the orientation of the easy axis. In addition one can also see the merge of the wave hills that was observed in the measured system matrices. However, in direct comparison with the measured system matrix, one can see that the direction of the tilt is homogeneous while the measurement shows a spatially dependent tilt. One attempt could be to assume that there is a homogeneous distribution of the easy axis in each voxel, which can be simulated by taking the mean over all simulated angles. But as is shown in figure 2, applying the mean leads to a similar pattern as observed for the equilibrium model A (see figure 1).

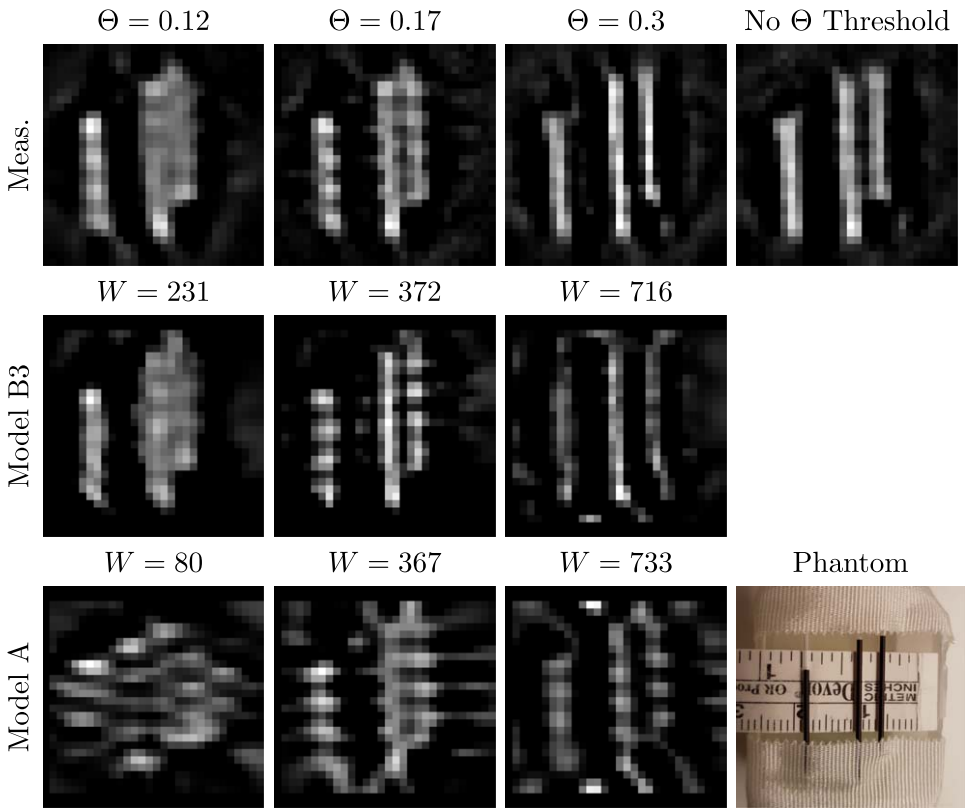

Figure 6. Reconstruction results of measured phantom data using three different system matrices: the measured system matrix, the matrix based on the equilibrium model A, and the system matrix obtained from the Néel model B3 for $g_{K_{\text{anis}}} = 1250\ \text{Jm}^{-3}$. Each reconstruction uses the same regularization parameter $\lambda = 10^{-7}$ and the same number of 10 Kaczmarz iterations. The threshold Θ is varied between 0.12 and 0.3. The resulting number of matrix rows W is given above the pictures for the models A and B3. For the measured system matrix, the same rows as for model B3 are selected. In the upper right corner, the reconstruction result for the measured system without Θ threshold is shown. In that case the number of matrix rows is $W = 833$.

The results from the spatially homogeneous anisotropy distribution motivate the usage of an space-dependent anisotropy distribution. In order to make the tilting orientation-dependent, we let the easy axis be parallel to the selection field vector. The results are shown in figure 3. One can see that the introduction of the spatially inhomogeneous easy axis and anisotropy constant does indeed introduce the two effects observed in the measurements: first a tilting effect and second a merging of the wave hills. With increasing anisotropy gradient, the effect gets stronger and starts already at the center. For small gradients, the effect is only visible in outer regions. For $g_{K_{\text{anis}}} = 1250\ \text{Jm}^{-3}$ we find the highest similarity compared to the measurement, which is also supported by the mean NRMSE shown in figure 3.

After choosing the model and optimal parameters (as described in section 7), we next make a more detailed comparison of model and measurement. Figure 4 shows various system matrix rows of the Néel model B3 in comparison with the equilibrium model and the calibration for various mixing factors and the x receive channel. One can see that the Néel model B3 much better describes the measurement than the equilibrium model. To support this observation, the figure also shows difference images. Just for $m_x = 1, 2$ and $m_x = 0$ the pattern still looks slightly different and the error is similar for both models. To quantify the differences we calculate the NRMSE for $m_x = 0, \ldots, 9$ and $m_y = 0, \ldots, 9$ which are shown in figure 5. The data confirms that the Néel model has lower error than the equilibrium model for most of the mixing factors. In particular for $m_x > m_y$ the error is much lower. For $m_x \ll m_y$, however, the error increases and there is no clear advantage of the Néel model.

Reconstruction results for the phantom data are shown in figure 6. One can see that the Néel model achieves a similar image quality as the calibrated system matrix. As expected the results are closer to each other if the threshold Θ is decreased. For large thresholds, the Néel model B3 results in artifacts at the boundaries of the FoV. The equilibrium model A shows a much worse image quality, which underlines, why it is usually not used in practice.

9. Discussion

The results show that the physics of a multi-dimensional MPI experiment can be approximately modeled by solving the Fokker–Planck equation considering Néel rotation with a spatially inhomogeneous anisotropy. Since

the simulation of the Néel model is computational expensive we did not fully optimize the set of unknown parameters yet. One can expect that the accuracy of the model increases even further when considering a particle size distribution and optimizing the probability density function of the particles. Instead of the ad hoc choice of a linear increasing gradient anisotropy (which implicitly assumes no anisotropy at the origin) it seems also promising to optimize the shape of the space-dependent anisotropy constant and easy axis. Furthermore, determining different optimal parameters for subsets of frequencies might also lead to improved accuracy due to an increased generality of the model which can particularly be beneficial for heterogeneous particle systems.

However, the proposed model can be rather interpreted as an approximate model than a physical model. A full physical model needs to take into account an anisotropy constant distribution as well as a time-dependent distribution of the particles' easy axis describing the probability that in a large ensemble of particles one particle's easy axis points in a certain direction on the S^2 (at a certain point in time). The latter distribution would be a result of a full physical model taking into account the coupling of Brownian and Néel rotation in ferrofluids. The relationship between a full physical model and the proposed approximate model remains future research.

The next step towards a more precise physical model could be to consider a coupled Brownian and Néel rotation model as for example has been derived in [17] but has not yet been validated on real data.

The strengths of using a model compared to using a calibration are manifold. We see the prime advantage that it allows to decouple the magnetic field sequence from the particle behavior. This enables using the same model and evaluating it under different field conditions (different excitation-field amplitudes and gradient strength). The need for such an approach is even more pressing for multi-patch sequences where a multitude of similar but slightly perturbed system matrices need to be acquired since the fields show imperfections in space [26].

Another application is multi-contrast MPI [37–39]. Here, one requires system matrices for different states of the particles (e.g. different viscosity or temperature). Using an accurate model, it is possible to determine the required system matrices just by modifying the parameters in the model. Furthermore, the problem of multi-contrast MPI can be formulated in terms of a joint parameter identification problem.

Acknowledgments

TK acknowledges funding by the Deutsche Forschungsgemeinschaft (DFG, German Research Foundation)—project number 281474342/GRK2224/1 'Pi^3: Parameter Identification—Analysis, Algorithms, Applications' and support by the project 'MPI^{2}' funded by the Federal Ministry of Education and Research (BMBF, project no. 05M16LBA). TK acknowledges the financial support by the German Research Foundation (DFG, grant number KN 1108/2-1) and the Federal Ministry of Education and Research (BMBF, grant number 05M16GKA and 13XP5060B). The publication is also funded by the German Research Foundation (DFG, project no. 392323616) and the Hamburg University of Technology (TUHH) in the funding programme Open Access Publishing.

ORCID iDs

T Kluth https://orcid.org/0000-0003-4814-142X
P Szwargulski https://orcid.org/0000-0003-2563-9006
T Knopp https://orcid.org/0000-0002-1589-8517

References

[1] Gleich B and Weizenecker J 2005 Tomographic imaging using the nonlinear response of magnetic particles *Nature* **435** 1214–7
[2] Sedlacik J, Frölich A, Spallek J, Forkert N D, Faizy T D, Werner F, Knopp T, Krause D, Fiehler J and Buhk J-H 2016 Magnetic particle imaging for high temporal resolution assessment of aneurysm hemodynamics *PLoS One* **11** e0160097
[3] Vaalma S, Rahmer J, Panagiotopoulos N, Duschka R L, Borgert J, Barkhausen J, Vogt F M and Haegele J 2017 Magnetic particle imaging (mpi): experimental quantification of vascular stenosis using stationary stenosis phantoms *PLoS One* **12** e0168902
[4] Ludewig P *et al* 2017 Magnetic particle imaging for real-time perfusion imaging in acute stroke *ACS Nano* **11** 10480–8
[5] Graeser M *et al* 2019 Human-sized magnetic particle imaging for brain applications *Nat. Commun.* **10** 1936–1936
[6] Yu E Y *et al* 2017 Magnetic particle imaging for highly sensitive, quantitative, and safe *in vivo* gut bleed detection in a murine model *ACS Nano* **11** 12067–76
[7] Knopp T, Gdaniec N and Möddel M 2017 Magnetic particle imaging: from proof of principle to preclinical applications *Phys. Med. Biol.* **62** R124
[8] Kruzík M and Prohl A 2006 Recent developments in the modeling, analysis, and numerics of ferromagnetism *SIAM Rev.* **48** 439–83
[9] Kluth T 2018 Mathematical models for magnetic particle imaging *Inverse Probl.* **34** 083001
[10] Weizenecker J, Gleich B, Rahmer J and Borgert J 2010 Particle dynamics of mono-domain particles in magnetic particle imaging *Magnetic Nanoparticles* (Singapore: World Scientific) pp 3–15
[11] Yoshida T and Enpuku K 2012 Nonlinear behavior of magnetic fluid in brownian relaxation: numerical simulation and derivation of empirical model *Magnetic Particle Imaging* ed T M Buzug and J Borgert (Berlin: Springer) pp 9–13

[12] Weizenecker J, Gleich B, Rahmer J and Borgert J 2012 Micro-magnetic simulation study on the magnetic particle imaging performance of anisotropic mono-domain particles *Phys. Med. Biol.* **57** 7317
[13] Yoshida T, Enpuku K, Dieckhoff J, Schilling M and Ludwig F 2012 Magnetic fluid dynamics in a rotating magnetic field *J. Appl. Phys.* **111** 053901
[14] Yoshida T, Othman N B and Enpuku K 2013 Characterization of magnetically fractionated magnetic nanoparticles for magnetic particle imaging *J. Appl. Phys.* **114** 173908
[15] Rogge H, Erbe M, Buzug T M and Lüdtke-Buzug K 2013 Simulation of the magnetization dynamics of diluted ferrofluids in medical applications *Biomed. Tech.* **58** 601–9
[16] Reeves D B and Weaver J B 2014 Approaches for modeling magnetic nanoparticle dynamics *Crit. Rev. Biomed. Eng.* **42** 85–93
[17] Weizenecker J 2018 The Fokker–Planck equation for coupled Brown–Néel-rotation *Phys. Med. Biol.* **63** 035004
[18] Ludwig F, Eberbeck D, Löwa N, Steinhoff U, Wawrzik T, Schilling M and Trahms L 2013 Characterization of magnetic nanoparticle systems with respect to their magnetic particle imaging performance *Biomed. Tech.* **58** 535–45
[19] Yoshida T, Matsugi Y, Tsujimura N, Sasayama T, Enpuku K, Viereck T, Schilling M and Ludwig F 2017 Effect of alignment of easy axes on dynamic magnetization of immobilized magnetic nanoparticles *J. Magn. Magn. Mater.* **427** 162–7
[20] Martens M A, Deissler R J, Wu Y, Bauer L, Yao Z, Brown R and Griswold M 2013 Modeling the Brownian relaxation of nanoparticle ferrofluids: comparison with experiment *Med. Phys.* **40** 022303
[21] Deissler R J, Wu Y and Martens M A 2014 Dependence of Brownian and Néel relaxation times on magnetic field strength *Med. Phys.* **41** 012301
[22] Enpuku K, Bai S, Hirokawa A, Tanabe K, Sasayama T and Yoshida T 2014 The effect of neel relaxation on the properties of the third harmonic signal of magnetic nanoparticles for use in narrow-band magnetic nanoparticle imaging *Jpn. J. Appl. Phys.* **53** 103002
[23] Shah S A, Reeves D B, Ferguson R M, Weaver J B and Krishnan K M 2015 Mixed brownian alignment and Néel rotations in superparamagnetic iron oxide nanoparticle suspensions driven by an ac field *Phys. Rev.* B **92** 094438
[24] Graeser M, Bente K, Neumann A and Buzug T M 2016 Trajectory dependent particle response for anisotropic mono domain particles in magnetic particle imaging *J. Phys. D: Appl. Phys.* **49** 045007
[25] Weizenecker J, Borgert J and Gleich B 2007 A simulation study on the resolution and sensitivity of magnetic particle imaging *Phys. Med. Biol.* **52** 6363–74
[26] Szwargulski P, Möddel M, Gdaniec N and Knopp T 2018 Efficient joint image reconstruction of multi-patch data reusing a single system matrix in magnetic particle imaging *IEEE Trans. Med. Imaging* **38** 932–44
[27] Knopp T, Sattel T F, Biederer S, Rahmer J, Weizenecker J, Gleich B, Borgert J and Buzug T M 2010 Model-based reconstruction for magnetic particle imaging *IEEE Trans. Med. Imaging* **29** 12–8
[28] Knopp T, Biederer S, Sattel T F, Rahmer J, Weizenecker J, Gleich B, Borgert J and Buzug T M 2010 2D model-based reconstruction for magnetic particle imaging *Med. Phys.* **37** 485–91
[29] Kluth T and Maass P 2017 Model uncertainty in magnetic particle imaging: nonlinear problem formulation and model-based sparse reconstruction *Int. J. Magn. Part. Imaging* **3** 1707004
[30] Knopp T, Biederer S, Sattel T, Weizenecker J, Gleich B, Borgert J and Buzug T M 2009 Trajectory analysis for magnetic particle imaging *Phys. Med. Biol.* **54** 385–97
[31] Goodwill P W and Conolly S M 2010 The x-space formulation of the magnetic particle imaging process: 1D signal, resolution, bandwidth, SNR, SAR, and magnetostimulation *IEEE Trans. Med. Imaging* **29** 1851–9
[32] Rahmer J, Weizenecker J, Gleich B and Borgert J 2009 Signal encoding in magnetic particle imaging *BMC Med. Imaging* **9** 4
[33] Kluth T and Jin B 2019 Enhanced reconstruction in magnetic particle imaging by whitening and randomized SVD approximation *Phys. Med. Biol.* **64** 125026
[34] Rahmer J, Weizenecker J, Gleich B and Borgert J 2012 Analysis of a 3D system function measured for magnetic particle imaging *IEEE Trans. Med. Imaging* **31** 1289–99
[35] Knopp T and Hofmann M 2016 Online reconstruction of 3D magnetic particle imaging data *Phys. Med. Biol.* **61** N257
[36] Them K, Kaul M G, Jung C, Hofmann M, Mummert T, Werner F and Knopp T 2016 Sensitivity enhancement in magnetic particle imaging by background subtraction *IEEE Trans. Med. Imaging* **35** 893–900
[37] Rahmer J, Halkola A, Gleich B, Schmale I and Borgert J 2015 First experimental evidence of the feasibility of multi-color magnetic particle imaging *Phys. Med. Biol.* **60** 1775–91
[38] Möddel M, Meins C, Dieckhoff J and Knopp T 2018 Viscosity quantification using multi-contrast magnetic particle imaging *New J. Phys.* **20** 083001
[39] Shasha C, Teeman E, Krishnan K M, Szwargulski P, Knopp T and Möddel M 2019 Discriminating nanoparticle core size using multi-contrast MPI *Phys. Med. Biol.* **64** 074001